Numerical Investigation of Parietal Pressure Distribution on NACA0012 Wing Controlled by Micro-cylindrical Rod Arranged in Tandem

LARABI Abderrahim[a], PEREIRA Michael[b], RAVELET Florent[b], AZZAM Tarik[a], OUALLI Hamid[a], MENFOUKH Laiche[a], BAKIR Farid[b,*]

[a] *Laboratoire de Mécanique des Fluides, Ecole Militaire Polytechnique, BP 17 Bordj El-Bahri 16214, Algiers, ALGERIA*
[b] *Arts et Metiers Institute of Technology, CNAM, LIFSE, HESAM University, F-75013 Paris, FRANCE*

Abstract

The aim of this study is to investigate the influence of disturbed freestream flow by a small cylinder on the laminar separated boundary layer over NACA0012 wing operating at a Reynolds number of $Re_c = 4.45 \times 10^5$. A detailed parametric investigations for the rod are performed using numerical simulations coupled with transition sensitive closure model ($\gamma - \tilde{Re}_{\theta,t}$) seeking for the optimal passive control parameters. Firstly, the use of such steady RANS model has been successfully accurate in capturing the separation induced transition on the baseline wing suction surface. Secondly, the rod location was scaled according to the formation length of vortices behind the micro-cylinder for which the aerodynamic loads are very sensitive. The effects of three rod diameter ratios ($d/c = 0.67\%$, 1.33% and 2%) on the laminar separation bubble and aerodynamic performances were examined. It was observed that the qualitative analysis of the flow structures revealed the mechanisms of the control device for the aerofoil performance improvements in which the rod wake exerted considerable effects on LSB size, pressure coefficient and flow streamlines. Particularly, it contributes to eliminate the boundary layer separation with pronounced decrease of 75% by energizing the shear layer over a significant extent, resulting in a mean drag dropping of 73% at 12° incidence, and a lift enhancement of about 23% at 15°.

Keywords: Laminar separated flow; SST transition model; Passive flow control; Bodies' wake interaction; Laminar separation bubble, Drag reduction; Lift enhancement.

1. Introduction

The laminar separation bubble is one of major issues met in several industrial applications in particular, those operating at low Reynolds number such us, UAV (Unmanned Air Vehicle), Micro Air Vehicle, race cars and even wind turbine. The boundary layer transition mechanism from laminar to turbulent state of such winged devices is deeply influenced by the aerodynamic characteristics of the wing in terms of boundary layer thickness, transition and separation locations, and wake thickness. In particular, the dynamic behaviour underlying behind these low Reynolds flows showed occurrence of slowly recirculating fluid characterized by a stationary rotating swirl known as a laminar separation bubble identified to be responsible of several negative effects on the overall aerodynamic performances, such as lift decreasing, drag increasing, aircraft stability reducing, vibration and even disturbing noise. This separation bubble is basically developed when the laminar boundary layer cannot overcome the local flow deceleration just coming after its acceleration. Hence, when it bypasses the leading edge of the wing at an incidence; the boundary layer peels off from the wall surface under the influence of an adverse pressure gradient. However, at higher Reynolds numbers this laminar boundary layer grows drastically to a turbulent state due to the presence of large inertial forces, and is therefore better able to overcome this adverse pressure gradient. After that, development of Kelvin-Helmholtz instabilities in this separated shear layer initiates turbulence which yields three-dimensional flow motions. This turbulent mixing is a complex process resulting in the separated streamline reattachment, through interactions between turbulent motions and the wing that incites the reattachment of the separated shear layer to the aerofoil surface, leaving an enclosed region of dead recirculating air. Therefore, understanding the physics involved in this phenomenon and possibility to control the resulting bubble are determinant for efficient engineering design. A review on laminar separation bubbles is presented by [35] where effects of Reynolds number on the laminar separation bubble occurrence on an aerofoil are discussed. The bubble is observed to appear for a Reynolds number ranging in between $[6\times10^4 - 6\times10^6]$. [29] introduced a theoretical model characterizing the laminar separation bubble in which he advocated a way of depicting the different critical points describing the LSB throughout the on-surface pressure measurements. The analysis clearly shows that pres-

*Corresponding author
Email address: farid.bakir@ensam.eu (BAKIR Farid)

sure distribution on the suction side remains fairly constant when the laminar boundary layer separates, after that the boundary layer reattaches to the surface when shear layer transition is triggered as revealed by drastically pressure increase. [39] used numerical simulations to compare between averaged over time and instantaneous flow-field near the aerofoil surface close to the separation region obtained by RANS-LES turbulence model. Their main results show typical Kelvin-Helmholtz instabilities in the shear layer is twisting into vortices that force the separated flow to stick towards the wall surface leading to a bubble shape in the time averaged outcome. In experimental studies, [40] conducted a hot wire investigation on the suction side of a wing at low Reynolds number which showed that a transient boundary layer can reattach to form a bubble and then continues downstream evolving into fully turbulent state. [13] conducted time averaged and instantaneous PIV experiments to provide information about transient behaviour of the laminar separated flow on low speed NASA GA (W-1) aerofoil at a Reynolds number of 7×10^4 based on the chord length. It is found that the bubble appears only when the incidence is in the range $[8^\circ - 11.8^\circ]$. Above this range at around 12° the pressure gradient becomes to be so significant to induce sudden bubble burst causing the aerofoil complete stalling. The authors reported also that LSB moves upstream towards the leading edge as the incidence increases in such a way its overall length remains unchanged. The laminar portion of this bubble, however, slightly extends in size, and the turbulent portion shrinks with the increasing angle of attack. By the same way, experimental results presented by [12] in form of PIV measurements at low Reynolds number flow around SD7003 aerofoil considering laminar separation bubble formation, pointed out the existence of a shear layer rolling up into a vortex sheet in the separated boundary layer originating from the presence of Kelvin-Helmholtz instabilities just after triggering of the boundary layer transition.

At the meantime, laminar separated flow control over aerofoils at moderate Reynolds numbers has gathered widespread research interest over decades, aiming to enhance their performances. A literature review on flow control shows existence of several techniques to manoeuvre a boundary layer, either in purpose of flow separation postponement so that the flow remains attached to the aerofoil surface, or to achieve lift enhancement, drag decreasing and noise damping. In respect to flow control techniques, these are categorized into two major classes: active and passive techniques. [9] added a reactive class to the above and showed up more specific ways of control depending upon the sought main goal. Many works have attempted to control the unfavourable phenomena that destroy the aerofoils aerodynamic efficiency. Suction and blowing are the most popular adopted active flow control. Although their benefits are obvious in terms of lift enhancement, drag reduction and stall delay as shown in [8] numerical investigations, the high cost, geometrical complexity and even energy consuming are most of their inherent weakness. Hence, naturally, a good flow control technique needs to be simple to implement, cheap and keeping the overall geometry unchanged. For these reasons, the so-called passive control techniques are the most widely used for simplicity, affordness and do not require any external energy supplying. Several numerical and experimental studies have shown up the effectiveness of such simple devices to control laminar separated flows around different aerofoils. [31] focused their numerical investigation on both passive and active on-surface vortex generators used to control the flow separation over NACA0012 aerofoil under conditions of $Re_c = 10^5$ and 6° incidence angle. The results showed a reduction of the separation zone over a significant extent up to 80% when the passive vortex generator is added. On the other hand, the active vortex generator made the separation zone almost to vanish in the time averaged flow results. However, this control technique did not impart drag reduction neither lift enhancement. [11] carried out numerical simulations to consider the effect of self-adapting flexible flaps on flow separation over NACA0012 aerofoil at moderate Reynolds number. The results showed a large modification of flow structure when elastic flap deforms under fluid-structure interaction forcing the wake to reduce in size and to lower intensity for shedding vortices. This resulted in a maximum lift enhancement of 69.49% for variable length flaps. Another passive control method was proposed by [37] aiming to investigate the aerodynamic characteristics of low Reynolds number flow over NACA0018 aerofoil. They have conducted numerical investigations using $k - \omega$ SST turbulence formulation over a wing model having a cavity on its suction side at various locations where a trapped vortex is acting as passive flow control technique. The geometry of the cavity and its aspect ratio is optimized seeking for higher performances. Elliptical cavity is more promising in enhancing the wing performance, whereas, circular one gave better lift to drag ratio when it is placed near the TE only. Leading edge protuberances is another technique adopted recently for aerofoil laminar flow control. The effectiveness of such vortex generator on the overall performance of S823 wind turbine model was highlighted from the numerical and experimental outcomes conducted by [34] at 2×10^5 Reynolds number. They postulated the main part of tubercles in smoothening and mitigating the stall effects to higher incidences which widen the scope of engineering operations for this modified wing. Moreover, the technique offered an additional increase of 19.38% in the overall aerodynamic efficiency. The control effect of permeable leading edge of NACA008 wing at moderate Reynolds number of 3.45×10^5 was illustrated recently by [2]. Despite its structure complexity, this method showed a strong influence on the aerodynamic coefficients where an improve of 65% in lift to drag ratio can be achieved.

The studies discussed above are mostly based on classical control techniques that introduce geometrical changes to the body itself. Lately, another passive flow control

method has gathered considerable attention in many engineering applications. It consists of an off-surface control element located far away from a body interacting with its boundary layer. This concept was first inspired each of these authors ([33]; [16]; [17]; [15]) who have suggested a control method of the separated shear layer from bluff bodies by placing a cylindrical rod in tandem arrangement in the upstream crossflow. The idea consisted in forcing the free shear layer to reattach on the body surface. This technique was applied to a cylinder, flat plate, square prism, diamond arranged square prism in order to investigate the flow response to this control method. The outcome recorded a pressure drag reduction of 63%, 30%, 75% and 34% respectively to each bluff body compared to the baseline bodies. Similar observations have been recently reported by [10] in their DNS investigations to supress the vortex shedding of a square cylinder by small control rod. A remarkable reduction of almost 15% in the mean drag coefficient was achieved. As for laminar separated flow over slender bodies, [42] examined numerically the wake body interaction between a cylinder placed in the near wake of NACA4412 aerofoil for a Reynolds number of 200 based on the cylindrical body diameter. The effect of the profile incidence, lateral and longitudinal distances between the two bodies in tandem arrangement is focused on the unsteady aerodynamic forces and carefully examined the vortex patterns of the cylinder along with its shedding frequencies. The main outcomes indicate a significant impact on the aerodynamic loadings, vortex patterns and shedding frequencies acting on the cylinder with an upstream streamlined body. In the same manner, [41] experimentally investigated aerodynamic performances of a cylinder placed downstream a NACA4412 aerofoil at chord based low Reynolds number ranged between $[1.47\times10^4 - 1.4\times10^5]$. They pointed out an abrupt decrease in both lift and drag forces as the side distance is increased. Furthermore, an exhaustive review on effects of wakes interaction and shedding frequencies between the added bluff body and the cambered aerofoil arranged in tandem in the cross flow was given by [3]. The experiments were carried out using the hot-wire anemometry. The findings highlighted the global physical involved phenomena when the aerofoil wake interact with the cylinder body. This mutual interference led to a significant change in Strouhal number values of both obstacles and the vortex patterns depending upon the spacing between them. Also, from an acoustic view, an LES based CFD analysis was performed by [36] to investigate the effect of turbulence generated by a rod of 10 mm in diameter place in front of wavy leady edge wing on its broadband noise for Reynolds number of 3.97×10^5. Results showed the fluctuations of lift and drag coefficients are damped out by 65.4% and 71.4% respectively causing a substantial reduction in the mean noise of 9.5 dB. Moreover, this was encouraged recently by [21] numerical study aiming to supress the far field noise generated by high lift 30P30N aerofoil model. They demonstrated that when the boundary layer control parameters are carefully set, the broadband noise is pronouncedly decreased by 24 dB and the flow field fluctuations are damped.

The previously investigated rod scales were mainly above 10% of the aerofoil characteristic length which led to a significant increase in the total drag of these systems. Therefore, a much smaller element scale was selected in case of such slender body's flow control. It was reported from [30] experimental investigations, that a micro-riblets placed on the suction side of a Riso aerofoil-based wing was used to assess its aerodynamic performances at wide range of angles of attack. They showed a significant drag reduction of 29.7% and 54% for Reynolds numbers of 2.02×10^5 and 1.4×10^5 respectively, which occurred at 7° incidence. [38] also used the concept of tiny structure to control the separated flow over horizontal axis wind turbine blade. It was found that for the optimum micro-cylinder parameters, the wind turbine power was increased by almost 74% without affecting its stability. Up to this, most of the related works on off-surface vortex generators were focused on either lift enhancement or drag reduction. [24] have used an off-surface cylindrical rod as a passive device to control the laminar separation bubble on the suction side of an elongated bluff body. The cylinder was placed upstream in the vicinity of the leading edge of the studied body. Their experiments showed that for the optimum control rod configuration, the laminar separation bubble seemed to entirely vanish. With similar experimental approach, [7] has studied experimentally the laminar separation bubble flow mechanism at pre-stall regime for SD7062 aerofoil controlled by small rod of different diameters at Reynolds number of 3×10^4 placed on the suction side at various chordwise locations. The PIV results revealed significant reduction in the size of the laminar separation bubble for proper rod diameter and location, along with decrease in height of the boundary layer by 22% which is coherent with the correlated reduction of 34% in the eddies' turbulent energy in the flow.

Considering the mentioned studies, there was an attempt to either suppress the vortex shedding of bluff bodies or improve aerofoils general aerodynamic performance in terms of loading enhancement or noise damping with large scale rod dimensions control element. In this study, a micro cylinder off-surface vortex generator is used to assess the feasibility of such passive technique to control the laminar separation bubble (LSB) over the suction surface of NACA0012 aerofoil at moderate Reynolds number. It aims to establish the optimum size and location of the tiny cylinder to improve its aerodynamic performance. In addition, except for experimental approaches, an issue of using fully turbulent classical RANS models (Spallart-Almaras, $k-\epsilon$, $k-\omega$ SST) to study flows involving laminar-turbulent separation has emerged as they require LES or experimental backup to identify the separation point. Therefore, detailed parametric investigations are carried out using RANS based simulations with transition sensitive closure model formulation known as Transition SST ($\gamma - \tilde{Re}_{\theta,t}$)

to extract the optimal configuration related to the rod for laminar separated flow control and emphasize the importance of including transitional effect in the numerical model.

2. Numerical Method

2.1. Case Geometry

In this study, three-dimensional flow over a NACA0012 wing model controlled by a micro-cylindrical rod is considered to assess its effect on the overall aerodynamic performances of this aerofoil. The global dimensions of the case model along with geometrical arrangement adopted for the passive control element are sketched in Fig.1. A circular cross-section cylinder of various diameters ($d/c = 0.67\%$, 1.33% and 2%) is chosen to act as an off-surface vortex generator and placed at a distance, L upstream from the rod centreline in the perpendicular direction to NACA0012 aerofoil. First, preliminary experiments are performed in this work where the spacing between the two components of the system is scaled according to the corresponding formation length, l_f of the vortices behind the tiny cylinder at flow conditions of 43.3 ms^{-1} freestream velocity and Reynolds number based on the aerofoil chord length, $Re_c = 4.45 \times 10^5$. In accordance with [26] experimental investigation, for a given Reynolds number of $Re_d = 5931$ based on the micro cylinder diameter, the formation length is roughly in the order of $2 \times d$ (Fig.2). Based on this, the method of fixing rod location and its effect on the wing gain in terms of maximum lift to drag ratio is reported and rod diameter scaling effect on LSB is explored. Four values for the distance, L are explored aiming to determine the optimum value. The spacings are set to be equal to $1 \times d$, $2 \times d$, $3 \times d$ and $4 \times d$ which correspond to location states of before, in, after and faraway the formation zone respectively. The sensitivity of varying L on the total aerodynamic loads is explicitly shown in Table 1.

Table 1 Rod location analysis

Location	Baseline	Before formation zone	In formation zone	After formation zone	Faraway formation zone
L	$0 \times d$	$1 \times d$	$2 \times d$	$3 \times d$	$4 \times d$
$\frac{\left(\frac{c_L}{c_D}\right)_{max}}{\left(\frac{c_{L0}}{c_{D0}}\right)_{max}}$	1.00	0.95	1.04	1.12	0.91

For cases where the considered spacing is halved or doubled according to the formation length, a loss of 10% in lift to drag ratio is observed compared to the baseline wing which reflect a severe deterioration of its aerodynamic performances. Thus, these two situations are not preferred as either the interaction is very weak between the rod aerofoil system or higher drag that corresponds to wider system's wake. In one hand, as the gap is close to the formation length, l_f, the system recovers its aerodynamic performance with slight increase in the maximum lift to drag ratio. In the other hand, the advantage of setting the micro-cylinder at position of $L = 3 \times d$ is demonstrated. As in such circumstances, an important gain in total lift to drag ratio is clearly achieved. Thus, after such comprehensive consideration the spacing adopted for the remaining study is $3 \times d$ as higher performance of the wing can be achieved compared to other sets.

Figure 1: (a) 3D representation of the control set-up; (b) Schematic of the wing controlled by micro-cylinder placed at distance, L from the leading edge (flow moving left to right).

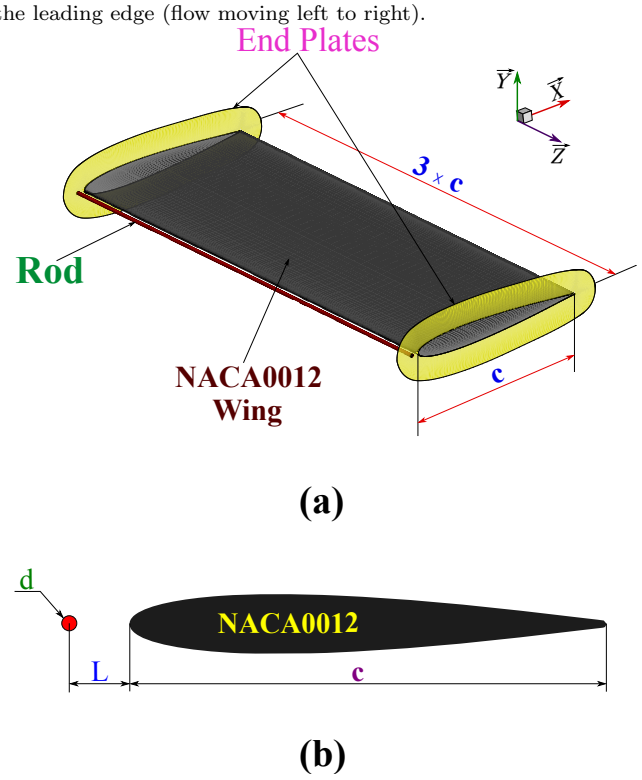

Figure 2: Vortex formation length, l_f as function of Reynolds number for a cylinder [26].

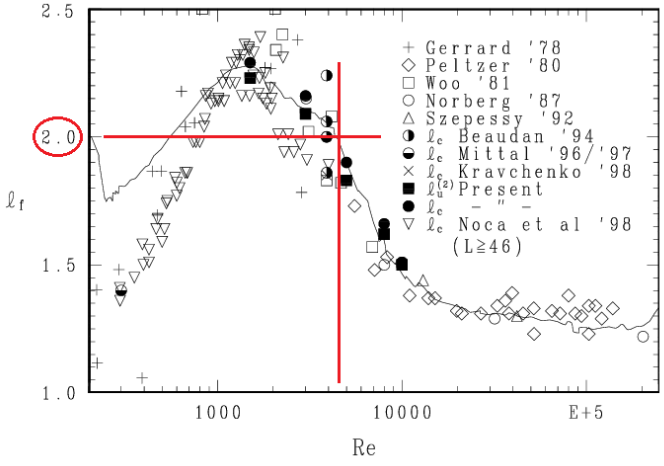

2.2. Computational Domain

To examine the sensitivity of the control element diameter scaling on the laminar separated flow and the aerodynamic performance of the cosidered wing model, detailed numerical investigations are presented in this paper. The three dimensions computational domain used to carry out this numerical study is illustrated in Fig.3. The coordinate system origin is placed at the leading edge of the wing. The overall domain dimensions are 6.3 m long, 3.6 m height and 0.465 m wide. The inlet boundary of the main domain is positioned 12 times the wing's chord length upstream from the centre point of the main aerofoil, and the rear boundary is extended giving a longitudinal length of $30 \times c$, where c is the wing's chord length. These domain extensions have been chosen in order to maintain a low blockage level and to ensure as little influence of all domain boundaries as possible which is demonstrated in [25] numerical study. A sensitivity test has been performed to optimize calculations in terms of time, memory and cost. The smallest size domain giving accuracy of less than 1% in terms of aerodynamic forces; with respect to each chosen downstream and lateral domain lengths; has a total height of $24 \times c$ and total length of $42 \times c$ with 2.7% blockage. The spanwise length, L_z is carefully chosen as a short spanwise width will fail to deliver results comparable with data from wind tunnels especially at high angles of attack. Thus, domain size dependence is inevitable to capture the 3D flow structures and ensure reliable results. For such analysis, a pair of symmetrical boundary conditions is set for both spanwise sides. Figure 4 shows that for spanwise length less than $2 \times c$ calculations give higher prediction for both coefficients. When further increasing this length, the variation tendency for both lift and drag seem to level off. Hence, a spanwise width of $3 \times c$ is selected for the 3D simulations. In addition, these domain characteristics are in good agreement when compared to literature. Based on the relevant numerical investigations carried out by [20] and [1], in which the effect of spanwise length of a computational domain on the accuracy of predicting the 3D flow structures past a circular cylinder was analysed. They showed that a minimum spanwise length of π times the characteristic length is required to predict a formation length that is in better agreement with experimental value. Thus, as this parameter plays an important role in rod distance parametric investigation, the adopted spanwise length for the current domain lies in the appropriate range.

2.3. Mesh Generation

The adopted grid topology for the considered computational domain is generated using ANSYS®-Meshing commercial software as illustrated in Fig.5. In order to construct a high-quality structured mesh, the domain is divided into several blocks allowing finer mesh in regions of susceptible eddies formation and coarse grid in far field regions. This strategy is performed using interface boundary conditions between different blocks. Furthermore, to

Figure 3: Computational domain topology and boundary conditions.

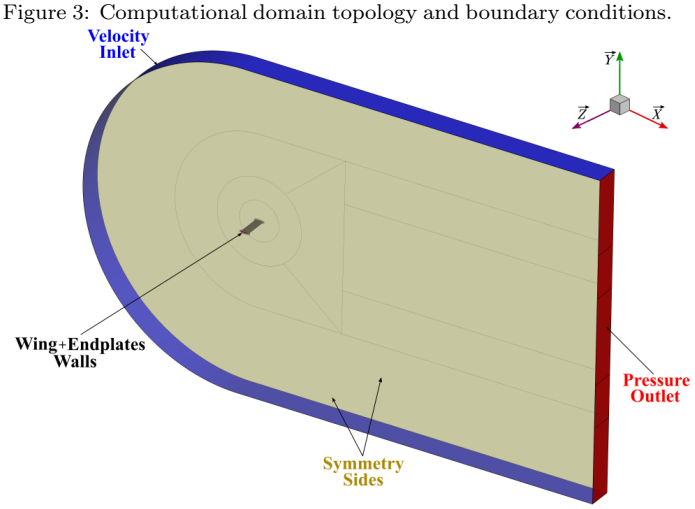

Figure 4: Variation of Lift and Drag coefficients for different spanwise lengths.

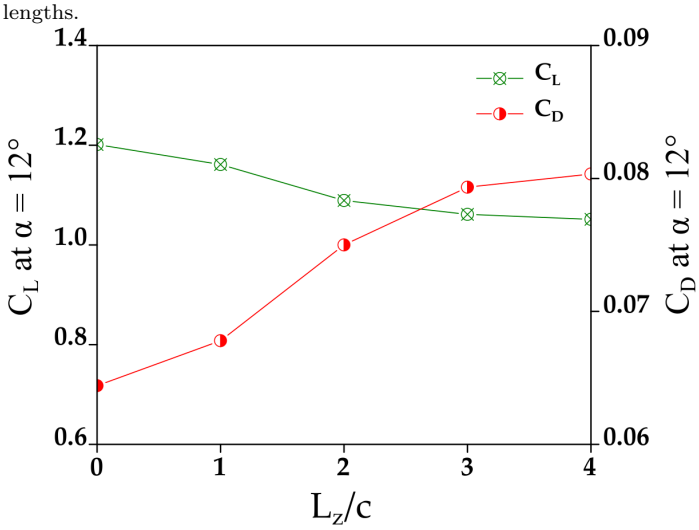

reduce the overall skewness and to ensure better cells orthogonality for the near wall grid elements as density is increased for the following mesh dependence analysis, an O-grid type topology is adopted and centred around both the wing and the cylindrical rod. This approach gives a smooth mesh transition in the leeward zone of the rod to the leading edge of the wing and allows a high resolution of the boundary layer while keeping relatively a low cell counts compared to C-grid type topology used in former similar studies which showed a reduction of about 50% in mesh size. The structured quadrilateral elements are chosen for the whole computational domain since they provide a high flexibility to control the cell counts with low memory consumption, accurate flow resolution and good flow alignment with respect to the mesh cells thus the overall rate of solution convergence is increased. Refined quadrilateral meshes are applied to critical flow zones where most

important phenomena affecting the flow structure around the wing are recorded. These zones are mainly the leeward side of the rod where the vortex shedding interacts with the leading edge of the wing ensuring thus minimization of the numerical viscosity effect responsible of artificial dissipation of the shedded vortices. In addition, a particular attention is paid to the mesh refinement at the aerofoil suction side to capture accurately flow features (Laminar Separation Bubble) involved in vicinity of the wing aerofoil including leading and trailing edges. In order to assess the significant impact of grid density on accuracy and convergence rate of the numerical solution, three different grid sizes are investigated for the mesh dependency analysis (Table 2). The coarse grid (MESH-1) contains 200 points on the suction side of the aerofoil, the fine mesh (MESH-2) with 450 grid points and the refined grid (MESH-3) has 640 points. It is noticed throughout sensitivity assessment for lift coefficient force that a deviation of about 4.59% is recorded for the coarse (MESH-1) and fine (MESH-2) meshes. While for the refined mesh (MESH-3), this difference in c_L drops to reach a value of roughly 0.56%. As a result, MESH-2 is retained and found to be suited to achieve accurately enough results for this numerical investigation. Another important grid independence was found to be in the exposure of turbulence models to y^+ values. Values of y^+ less than unity found to be necessary in order to capture transitional features of the flow on the suction side of the aerofoil by accurately modelling the boundary layer. A target value of 0.7 based on the freestream inlet velocity is applied to the entire wing surface and the cylindrical rod during pre-processing simulation case. After that, y+ distribution along the upper and lower surfaces of the aerofoil and around the cylinder circumference is checked in post-processing phase for all simulations and showed to be less than unity. A total of 15 inflation layers were chosen with a stretching ratio of 18% at the wall surface giving a prism layer thickness large enough to fit development of the boundary layer along with the separation bubble that may occur. As a result of this parametric strategy, a reasonable quality and sufficiently fine structured mesh is with solution-mesh independency condition satisfied.

Table 2 Grid independence analysis

Mesh	Nodes on Aerofoil	c_L at 10°	Error (%) with previous mesh
MESH-1	200	0.8636	-
MESH-2	450	0.9035	4.59
MESH-3	640	0.9086	0.56

2.4. Turbulence Model

The conventional turbulence models available for RANS formulation such as one equation Spalart-Allmaras model and two equations $k-\epsilon$ and $k-\omega$ models, do not include laminar effects especially for low Reynolds number flows, thus considering fully turbulence models in such studies is invalid assumption. Even though, DNS and LES methods solve turbulence with sufficient precision so that laminar and transition effects can be predicted, grid density and time resolution requirements are prohibitive and probably inappropriate to be used for industrial design purposes. This led to an attempt to include laminar transitional effects using damping functions in near wall regions to gain relatively good prediction of transition by diffusing freestream turbulence into the boundary layer. In addition, this strategy offers a good balance between grid density requirement and flow complexity. This model known as Transition Shear Stress Transport ($\gamma - \tilde{Re}_{\theta,t}$) introduced by [23] for low Reynolds number approach introduces a so-called viscosity limiter that reduces prediction of the wall shear stress thus it is more likely to get separation over smooth surface and results will give better agreement with experiments of separated flows. Several RANS turbulence models are used to investigate laminar separated flows at low Reynolds numbers. It is noticed that Transition SST model provided good prediction of pre and post stall behaviour for aerodynamic loads ([4]) and is in good agreement with correlating comparative wind tunnel experiments ([32]; [28]). Furthermore, this latter model proved its reliability in capturing flow interaction features between bodies and its high revelation of parietal pressure oscillations. According to what has been discussed so far, it seems that Transition SST turbulence model is capable of capturing accurately laminar separation with transition of the boundary layer on wings operating at low Reynolds flow regime, allowing to solve details inside the boundary layer when blending effectively between the standard $k-\omega$ in near wall regions and $k-\epsilon$ model in the far field. Hence, Transition SST model is adopted for all simulations which eventually increases the CPU time to about 22% whilst transition sensitive SST model formulation is used to model the laminar separation bubble near the leading edge when boundary layer transits form laminar to turbulent state, because this LSB is a dominant phenomenon when characterizing pressure distribution, on-surface flow structure and wall shear stress over the wing and therefore the overall aerodynamic loads of the wing. However, even though SST $k-\omega$ is inefficient in correlating a good prediction of flow features at moderate Reynolds, it shows a comparative correlation with wind tunnel experiments at very high angles of attack.

$$\frac{\partial(\rho k)}{\partial t} + \nabla\cdot(\rho\mathbf{U}k) = \nabla\cdot\left[\left(\mu + \frac{\mu_t}{\sigma_k}\right)\nabla k\right] + P_k - D_k \quad (1)$$

$$\frac{\partial(\rho\omega)}{\partial t} + \nabla\cdot(\rho\mathbf{U}\omega) = \nabla\cdot\left[\left(\mu + \frac{\mu_t}{\sigma_k}\right)\nabla\omega\right] + \frac{\gamma}{\nu_t}P_k - \beta\rho\omega^2 + 2(1-F_1)\frac{\rho\sigma_{\omega_2}}{\omega}\nabla k : \nabla\omega \quad (2)$$

Figure 5: (a) Schematic of the adopted mesh topology of the CFD domain (flow moving left to right); (b) Structured mesh around the rod close to the aerofoil; (c) Structured mesh close to the trailing edge of the aerofoil.

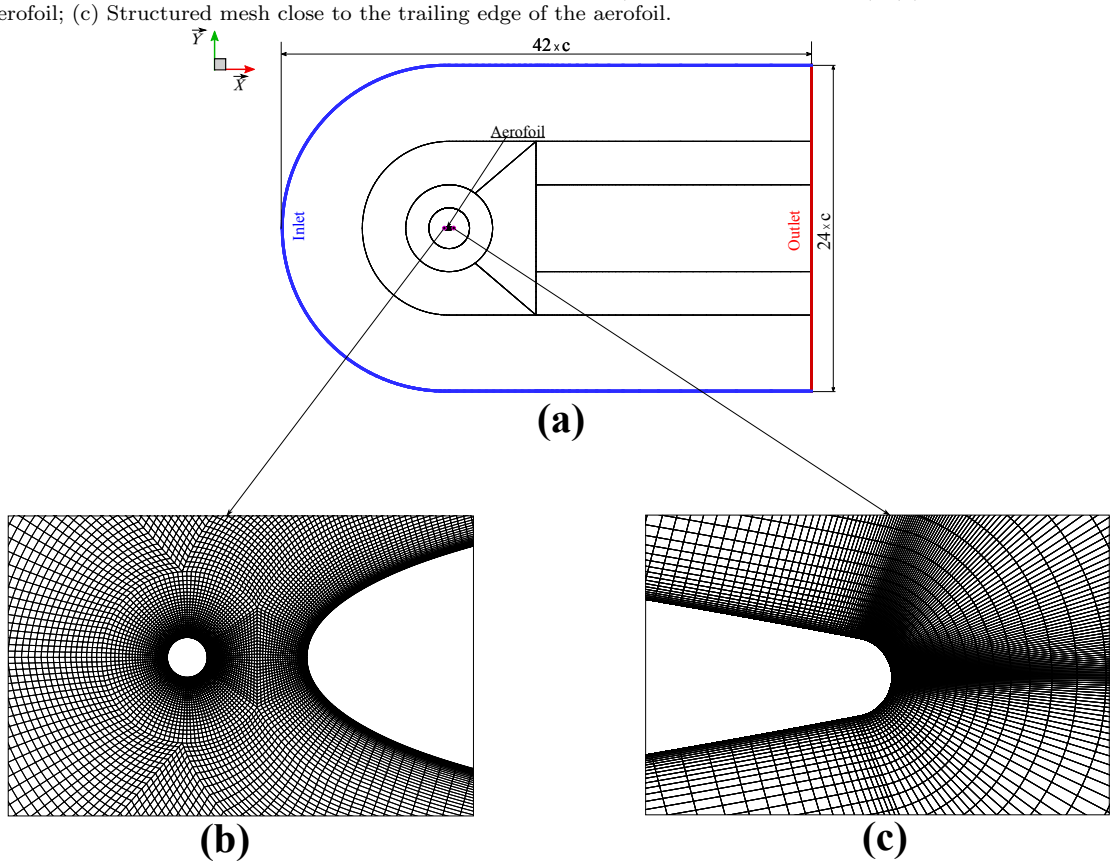

Where, $$\nabla k : \nabla \omega = \frac{\partial k}{\partial x_j}\frac{\partial \omega}{\partial x_j}$$

$$P_k \rightarrow P_k\, \gamma \qquad 0 \leq \gamma \leq\ 1 \tag{3}$$

$$D_k \rightarrow D_k\, min\left[max\left(\gamma,\ 0.1\right),\ 1.0\right] \tag{4}$$

$$F_1, new = max\left(F_1,\ F_3\right) \tag{5}$$

Where, $F_3 = e^{-(Re_y/120)^3}$ and $Re_y = \frac{\rho y\sqrt{k}}{\mu}$

The $\gamma - \tilde{R}e_{\theta,t}$ turbulence model still solves the transport equations for both k and ω quantities as $k-\omega$ SST does, which are otherwise identical with an exception for production, P_k and dissipation, D_k terms in kinetic energy (Eq.(1)) along with the blending function F_1 in specific dissipation rate (Eq.(2)) that controls the use of ω near the walls and ϵ far away. The production term, P_k is correlated with a turbulence intermittency, γ (Eq.(3)) bounded between values of 0 and 1, indicating physically the state of the flow locally by accounting for the percentage of time corresponding to the presence of turbulent fluctuations in the boundary layer. Where a value of 0 indicates that the flow is locally laminar hence close to the leading edge of the aerofoil and when γ saturates to a value of 1 the flow is fully turbulent. Notice that freestream flow contains turbulent kinetic energy and specific dissipation rate, thus γ should have a value of 1 at inlet boundary condition and freestream so that it will be represented by the fully $k-\omega$ SST model. Regarding the dissipation term, Dk it is limited by a min max limiter (Eq.(4)) calibrated to ensure that its value does not drop below 10% of its fully turbulent value when $\gamma = 0$, because even when the boundary layer is laminar with no production of turbulent kinetic energy, if is there any turbulence the wall still dissipate it by damping these turbulent fluctuations of the flow. In other hand, numerical tweak is used to correct the blinding function, F_1 to prevent it to take a value of 0 in the laminar boundary layer near the wall where normally takes a value of 1 allowing the Transition SST model to take its $k-\omega$ form of $k-\omega$ SST turbulence formulation rather than $k-\epsilon$ which is ineffective in the near wall regions particularly when the values of y^+ are very small. Hence, the blending function is limited; to prevent it to switch accidentally to 0 in the laminar region; by a new term defined by an exponential decay of a Reynolds number like term (Eq.(5)) governed by a square-root of turbulent kinetic energy which is very small in the laminar portion of the boundary layer making this new term to tend to 1.

$$\frac{\partial\left(\rho\gamma\right)}{\partial t} + \nabla\cdot\left(\rho\mathbf{U}\gamma\right) = \nabla\cdot\left[\left(\mu + \frac{\mu_t}{\sigma_\gamma}\right)\nabla\gamma\right] + P_\gamma - D_\gamma \tag{6}$$

$$P_{\gamma,1} = F_{length}\, C_{a1}\rho\, S\left(\gamma\, F_{onset}\right)^{0.5}\left(1 - C_{e1}\gamma\right) \tag{7}$$

$$\frac{\partial\left(\rho\tilde{R}e_{\theta,t}\right)}{\partial t} + \nabla\cdot\left(\rho\mathbf{U}\tilde{R}e_{\theta,t}\right) = \nabla\cdot\left[\left(\mu + \frac{\mu_t}{\sigma_{\theta,t}}\right)\nabla\tilde{R}e_{\theta,t}\right] + P_{\theta,t} \tag{8}$$

$$P_{\theta,t} = 0.03\frac{\rho}{t}\left(Re_{\theta,t} - \tilde{R}e_{\theta,t}\right)\left(1 - F_{\theta,t}\right) \tag{9}$$

In order to compute the values of γ in the flow field an additional standard transport equation for intermittency is solved (Eq.(6)). The production terms, P_γ is used to control the length of the transition region of the boundary layer by producing turbulent fluctuations and pushing γ to saturates at a value of 1 in the full turbulent region. This term takes the form of Eq.(7) characterized by two main terms F_{onset} and F_{length}, where the former is a switching function for the production of intermittency and the latter controls the rate of this production happens to be when F_{length} is large γ is produced quickly and saturates to 1 rapidly which shortens the length transition region. To assess the F_{onset}, the Transition SST model introduced another transported variable, $\tilde{R}e_{\theta,t}$ calculated everywhere in the computational domain (Eq.(8)). This variable connects the empirical correlations to the onset criterion of intermittency by calculating two local values $Re_{\theta,t}$ and $Re_{\theta,c}$ where transition occur and fluctuations begin to take place respectively. The source term, $P_{\theta,t}$ of Eq. (8) is included to force $\tilde{R}e_{\theta,t}$ to take its experimental value (proprietary of ANSYS®-Fluent 18.2 CFD code) specified at the inlet except near the wall where it is turned off allowing the freestream value of $\tilde{R}e_{\theta,t}$ to convect and diffuse toward the wall by introduction a blending function $F_{\theta,t}$ (Eq.(9)). Once $Re_{\theta,t}$ is computed F_{length} and F_{onset} are evaluated using algebraic relationships and when they are beyond certain threshold the source term, P_γ is switched on, hence production of intermittency γ will start for each cell ([19]; [22]; [5]).

2.5. Boundary Conditions

In addition to the domain sensitivity analysis conducted to set right dimensions of upstream, downstream, top and bottom boundaries of the computational domain, an appropriate implementation of boundary conditions needs to be carefully considered. This is achieved by splitting the domain boundaries into three distinct regions, velocity inlet, pressure outlet downstream and symmetry side boundaries. A velocity inlet type was specified as Dirichlet boundary condition at inlet boundaries in such a way that freestream velocity is set to maintain a chord-based Reynolds number at 4.45×10^5. The used method for freestream turbulence is by setting values of turbulent kinetic energy and specific dissipation rate at the inlet boundary condition, unless otherwise stated, as

$k = 2.53\ m^2s^{-2}$, $\omega = 151.55\ s^{-1}$ and an intermittency factor of 0.85 as dependence of flow features on γ values at the inlet was observed. These quantities are calculated based on empirical correlations related to SST $k-\omega$ turbulence model. The downstream domain boundary was prescribed as pressure-outlet boundary condition and set to a value of zero-gauge pressure as operating conditions of the working fluid are specified according to standard atmospheric pressure of 101.325 kPa and temperature of 288.15 K. In addition, an estimation of turbulent length scale of 10% the characteristic length is set at the pressure-outlet along with 5% backflow turbulence intensity. A stationary wall condition is adopted for both aerofoil and rod surfaces with no-slip boundary condition, hence, no turbulence production from the wall itself to the freestream flow. The two side boundaries of the computational domain are assigned to symmetry boundary condition which enforces to null the normal component of all flow variables gradient by acting as zero shear slip wall. This condition seems to be satisfactory as the computational domain is large enough to maintain these far boundaries at constant static pressure (Fig.3).

2.6. Solver and Numerical Schemes

[27] have shown that the laminar separation bubble does not involve any vortex shedding via their time-dependent numerical investigation of the laminar separated flow subjected to an adverse pressure gradient. As a motivation, three dimensional, incompressible, steady state, pressure based and segregated double precision numerical solver is adopted to conduct present simulations. All Steady RANS CFD runs were undertaken using the industry standard commercial CFD package known as ANSYS®- Fluent, Release 18.2. The code solves the Reynolds Averaged Navier Stokes equations in a finite volume environment with Message Passing Interface library parallelization. The Transition SST ($\gamma - \tilde{R}e_{\theta,t}$) four (4) equations turbulence closure model is adopted to model the Reynolds stresses term. The choice of this model is motivated by its ability to capture up to a good extent the separation bubble that occurs on the suction side of the wing which appeared to be harmful for its aerodynamic performances and also, has proven reliability in flows involving wake interactions. Pressure-Velocity field coupling is ensured using SIMPLE algorithm advantageous for problems requiring boundary layer high resolution. Spatial discretization of pressure term is treated by a standard interpolation scheme. Moreover, momentum diffusive terms, turbulent kinetic energy and specific dissipation rate equations are second-order central difference special discretization scheme and convection terms are treated using second-order upwind discretization scheme in space. Finally, the cell gradients of all variables are computed using weighted least square cell-based scheme. The initial flow field for all simulations is set according to predicted freestream inlet conditions. The different cases are computed for 50000 iterations where scaled residuals of all equations along with lift and drag coefficients of the wing are monitored to ensure adequate convergence. The overall computational time for every simulation to be converged was achieved in about 144 hours (wall clock) that led to reduction in the residuals of $O(6)$ (Fig.6). Afterwards, to ensure the convergence accuracy, both lift and drag coefficients are monitored to the extent in which they are fully converged as demonstrated in Fig.7 where solutions for all cases are continued until there is no variation in C_L and C_D which characterized by the horizontal asymptotic looks like.

Figure 6: Convergence history for scaled residuals.

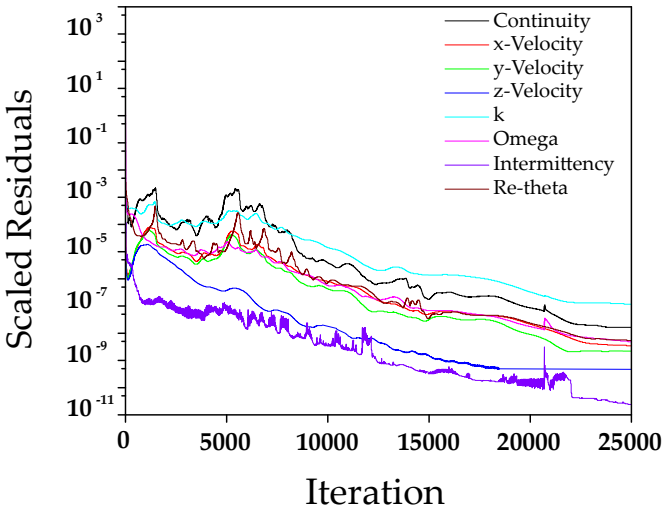

3. Results and Discussions

Simulations of the flow around the wing at various angles of attack ranging between $[0° - 24°]$ for a chord-based Reynolds number of 4.45×10^5. are carried out for both baseline and controlled configurations in order to understand how wing surface pressure are altered when a passive control method is introduced to enhance the overall wing aerodynamic performances at pre-stall and stall regimes.

3.1. Validation

For reason of results confidence, it is imperative to compare the obtained results from CFD simulations of the baseline wing with Wind Tunnel experiments to validate the numerical model adopted herein. Tests are carried out in an open jet closed circuit wind tunnel having circular test section of 600 mm in diameter. The wing model is NACA0012 aerofoil based with 150 mm chord length and 465 mm span giving a maximum blockage ratio of 6.4%. The forces acting on the wing under the stream are measured by aerodynamic balance composed of three masts $D\#1$, $D\#2$ and $D\#3$. The measurements range of each one is respectively $[-100\ N - +100\ N]$ for both $D\#1$ and $D\#2$ and $[-50\ N - +50\ N]$ for the last one. A mechanism for angle of attack variation is also incorporated with the

Figure 7: Lift and Drag coefficients convergence for angle of attack 14°.

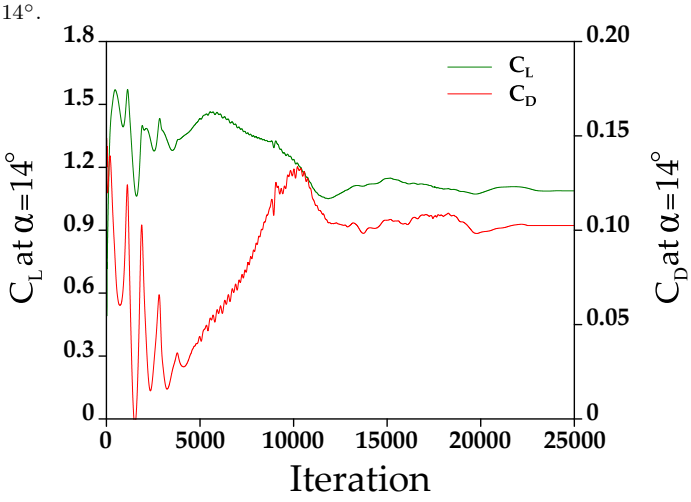

Figure 8: NACA0012 wing mounted on the three-components aerodynamic force balance.

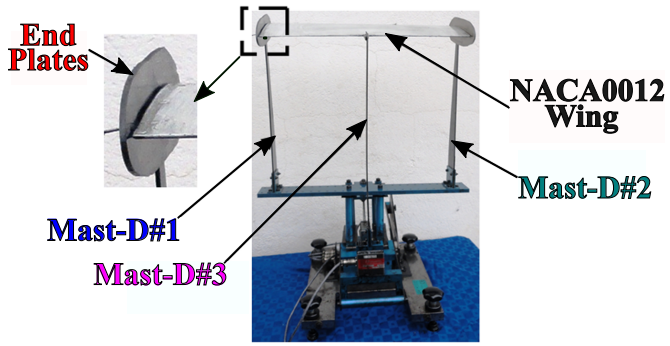

balance allowing α to be set between $[-20° - +40°]$ (Fig.8). The experiments for the baseline wing configuration used for CFD validation are obtained for a freestream velocity of 43.32 ms^{-1}, that corresponds to a Reynolds number based on the chord length of 4.45×10^5. The turbulence intensity for these flow conditions is 1%. Table 3 shows the error in the aerodynamic forces predicted by current numerical investigation when compared to CFD simulations of [14] and the wind tunnel results. It is noteworthy that deviations remain less than 8.28% in all instances except at 14° incidence where the wing stalls and making this region quite difficult to solve with turbulence modelling formulation of Navier-Stokes equations. Although simulations overpredict lift force coefficient the fact that the error is relatively consistent for each case, highlights that the overall trends shown by the numerical results are coherent with those occurring in the wind tunnel.

Table 3 Lift coefficient from CFD simulations and wind tunnel

•	c_L **at** 10°	c_L **at** 12°	c_L **at** 14°
Present work	0.9035	1.0613	1.0876
CFD [14]	0.8752	0.9801	1.025
Error (%)	**3.23**	**8.28**	**6.1**
Wind Tunnel	0.898	1.021	0.962
Error (%)	**0.61**	**4.0**	**13.05**

Figures 9 and 10 depict distribution of the parietal dimensionless distance, y^+, on both wing surfaces and the rod circumference. The average value seems to be largely less than unity in order of 10^{-1}. Thus, resolution of the boundary layer of the flow near both bodies is performed accurately enough throughout the grid used to conduct the different CFD simulations. Hence, spacing of the first cell from the wall is validated for this numerical study.

Figure 9: Wall y^+ distribution on the wing at 10° and 18° of incidence.

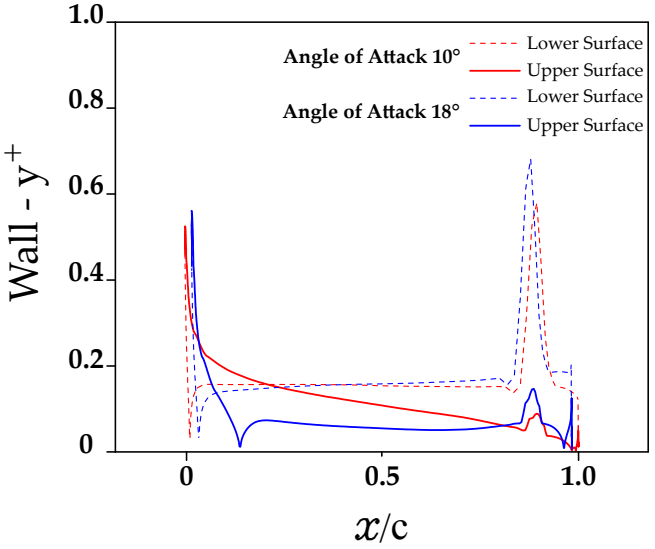

The comparison between CFD, experimental and literature data are shown in Fig.11. [18], [6] have presented wind tunnel experiments in which flow characteristics over NACA0012 aerofoil is deeply investigated at various Reynolds numbers and wide range angles of attack. The obtained results from numerical and experimental approach adopted in the current work are validate against these produced experimental data. As it is seen, for angles of attack less than 12° both CFD and experimental outcomes are in good agreement with the selected experimental data. The highest recorded error is less than 4% for lift coefficient and in the order of 5% in case of drag coefficient. Whereas, after stall angle, the numerical predicted results show a significant deviation from the current experimental data especially for lift coefficient, which can be attributed to the effect of close walls in experiments. On the other hand, lift coefficient from CFD gave satisfactory results as it is in better agreement with [18] experimental data.

In addition, statistical analysis between numerical predic-

Figure 10: Wall y^+ distribution over the micro-cylindrical rod at angle of attack of 16°.

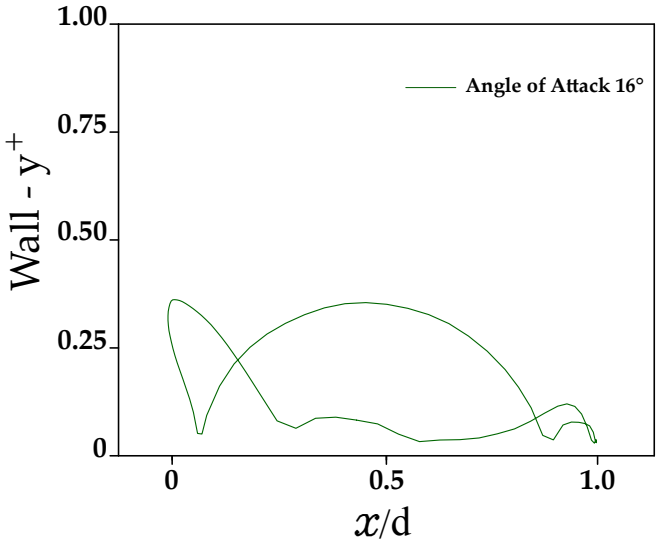

Figure 11: Comparison between the current CFD and experimental results with previous experimental data.

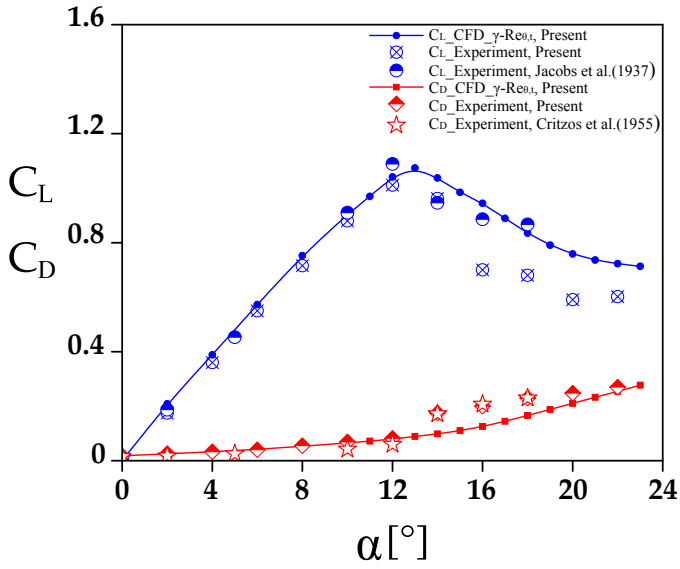

tions and experimental data is performed using Pearson correlation criterion. It consists of assigning a quality level for given data set, by measuring the linear correlation strength between two sets of data. The related coefficient, r is given by Eq.(10) as follow :

$$r_{X,Y} = \frac{cov(X,Y)}{\sigma_X \times \sigma_Y} \tag{10}$$

Table 4 summarises the values of the strength for possible linear correlation between the present obtained experimental as well as numerical prediction results and the experimental data taken from literature in terms of lift and drag coefficients. The main interpretation behind, r is that any value ranged between $[0.9 - 1]$ indicates the existence of a very strong correlation between the data sets. Thus, overall, CFD results and experimental measurements gave satisfactory prediction for both lift and drag coefficients and are comparative to experiments taken from literature.

Table 4 Pearson's coefficient for different data sets

	Present CFD vs. Present Experiment		Present CFD vs. Literature Experiment		Present Experiment vs. Literature Experiment	
	C_L	**C_D**	**C_L**	**C_D**	**C_L**	**C_D**
r	0.9743	0.9581	0.9935	0.9463	0.9797	0.9931

3.2. Baseline Flow Analysis

Figures 12 and 13 show variation of the aerodynamic coefficients, c_L and c_D, at low Reynolds number and various angles of attack for the baseline NACA0012 wing simulations along with a schematic of the flow patterns observed for each representative state. It is noticed that, for incidence ranged between $[2° - 13°]$ a monotonous linear increase in the lift coefficient relatively growing in a constant rate up to a maximum value depicted at $\alpha = 13°$. After reaching the peak, the value of c_L drops drastically at $\alpha = 14°$ showing turbulent stalling phenomenon of the boundary layer taking place as clearly illustrated by the schematic of the streakline patterns on the wing surface. The flow separation is led to move upstream causing the wing to stall. Above incidence of $\alpha = 20°$, the lift shows a tendency to be relatively constant. This is basically due to the main flow separation indicated by the presence of counter-rotating vortices on the suction side of the wing hence the post-stall is triggered. Regarding drag coefficient c_D, it remains almost unchanged for small angles of attack $[0° - 6°]$. Thereafter, it increases slightly in the meantime as the angle of attack is further changed possibly because of premature separation of the laminar boundary layer, followed by a significant rise for $\alpha = 14°$ indicating presence of turbulent stall of the boundary layer. By further increasing the angle of attack, the drag coefficient continues growing till a maximum value is attained at incidence 24°.

The streamline close to the wing surface is presented in Fig.14 to make a comparison between various angles of attack and the presence of flow separation on the upper surface of the aerofoil. It is believed that the nonlinearity in the lift curve slope is linked to presence of laminar boundary layer separation occurring at this low Reynolds number flow ($Re_c = 4.45 \times 10^5$). For an angle of attack between 0° to 8°, a separation bubble appears on the aerofoil suction side that travels from the trailing edge to the leading edge as the incidence is increased, leading effectively to a change in location of the transition line from laminar to

Figure 12: CFD lift coefficient for baseline case at varying AOAs.

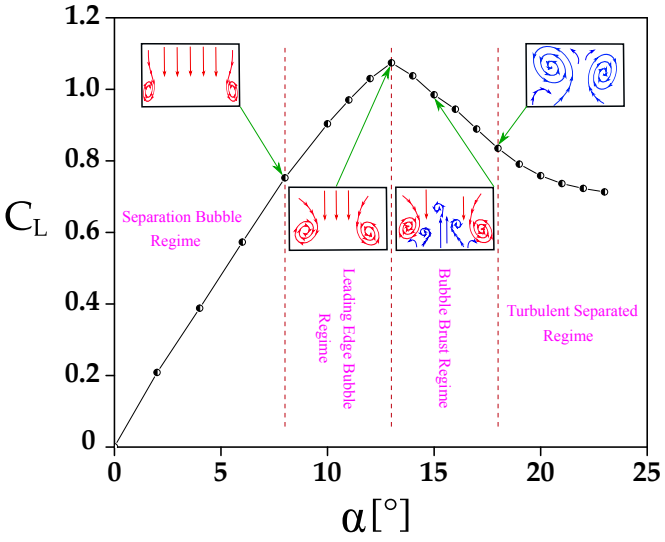

Figure 13: CFD drag coefficient for baseline case at varying AOAs.

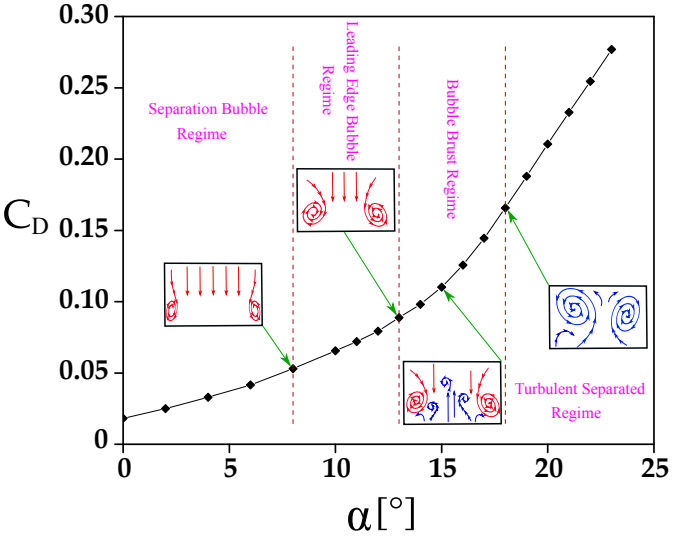

turbulent states. For $\alpha > 8°$, two separate phenomena are observed consisting in presence of a conventional trailing edge separation bubble formed along with the first bubble near the leading edge as the angle of attack increases till the point of complete separation on the upper surface of the wing representing the stall phenomenon, at around an angle of attack of $[10° - 12°]$. These two phenomena can explain the change in lift curve slope observed in Fig.12.

3.3. Effect of Passive Control on LSB

Three-dimensional development of the LSB on the wing upper surface is inferred from average pressure distribution analysis on suction side presented in Fig.15. Showing mean pressure rapid increasing along the chordwise direction. It can be seen from colour contrasts of pressure

Figure 14: Process of LSB migration at low Reynolds number of 4.45×10^5 for NACA0012 wing; arrows highlights the LSB location (flow moving left to right).

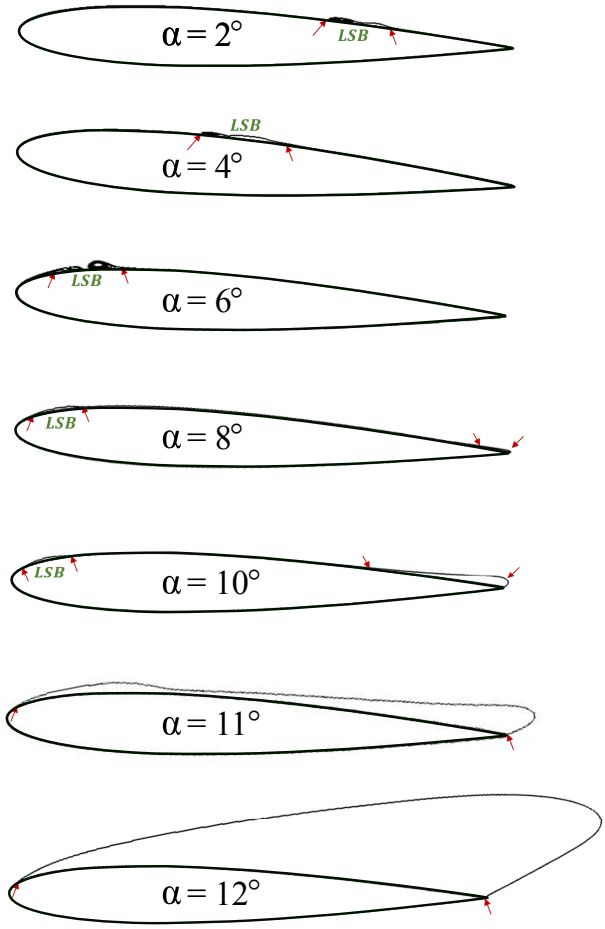

distribution, existence of three distinguished regimes characterizing the zone of laminar separation bubble observed for low Reynolds number flow, namely, laminar, transient and turbulent flow regimes. These three regions are limited by the following three characteristic lines as shown in Fig.15: Laminar separation line; Transitional line and Reattachment line. Effect of the passive control technique on development of the LSB is analysed and the most relevant results are presented in Fig.16. The figure depicts average pressure distribution contour on the upper surface of the wing at an incidence of $\alpha = 10°$. Comparing the two configurations side to side, baseline case and controlled case, it seems that the rod has significant influence on dimensions of the laminar separation bubble occurring on the suction side as a result of premature laminar boundary layer separation. Both regions, laminar and transitional, are influenced by presence of the rod wake. A significant reduction of approximately 50% in the laminar region is depicted by the three-dimensional average pressure distribution on the wing surface which yielding to a considerable enlargement of the transitional zone by approximately 30%. Thus, this vortex generator placed

Figure 15: LSB characterisation at flow conditions of $Re_c = 4.45 \times 10^5$ and $\alpha = 8°$ (flow moving top to bottom).

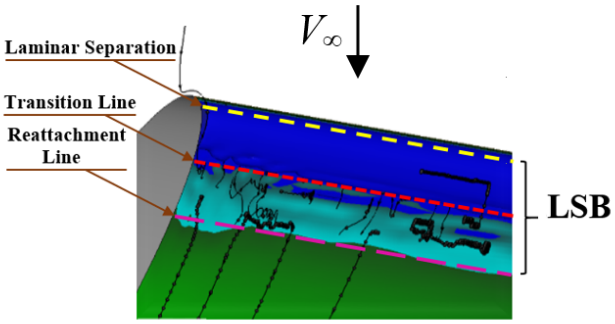

upstream the wing showed that LSB is extremely sensitive to the interaction between the rod wake and the aerofoil leading to a bubble size reduction that is considered to be harmful for the wing overall aerodynamic performances. Therefore, a promising enhancement in aerodynamic characteristics will certainly contribute to improve efficiency of such wings operating at low Reynolds numbers.

Table 5 Rod effects on LSB size

Angle of attack	5°	8°	10°
Size Reduction [%]	31.29	15.57	75

Figure 16: Effect of micro-cylinder rod on LSB dimensions at $\alpha = 10°$; (a) baseline case; (b) controlled case (flow moving left to right).

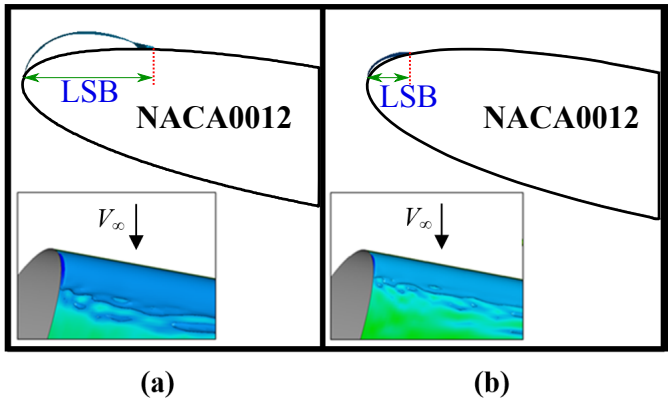

3.4. Effect of Passive Control on Parietal Pressure Distribution

Figure 17 demonstrates both friction lines and average pressure distribution on the wing upper surface. When incidence is null ($\alpha = 0°$), friction lines on the wall surface are uniform and flows in the same direction as that of the main incoming flow, starting from the leading edge towards the trailing edge. As the angle of attack is increased ($\alpha < 11°$), friction lines begin to lose their uniformity and smoothness behaviour. An instability is triggered on both ends of the trailing edge, indicating presence of a partial separation of the boundary layer, developing progressively from the trailing edge towards the leading edge. Furthermore, the average pressure gradually increases in the chordwise direction starting from the leading edge. It begins with a zone of depression at the leading-edge level indicated by a uniform and homogeneous coloured zone and keeps growing to a high-pressure region at the trailing edge. For the baseline configuration at $\alpha = 11°$, the depression zone is narrow on both ends of the leading edge, because the instability generated between endplates and aerofoil boundary layers mutually interact. This is much clearer through the friction lines distribution showing a pair of counter-rotating vortices swirling on the wing suction side. Consequently, partial turbulent stall of the main wing is triggered close to these regions. In case of controlled wing configuration, it shows, however, important changes noticeable on the mean pressure field as well as on the friction lines (Fig.17). Mainly, the depression region near the leading edge is getting uniformized in the spanwise direction starting from middle towards endplates. Another important outcome is revealed by new friction line patterns resulting from the control and consisting in the fact that the pair of vortices near endplates shrink in size making the incident flow more dominate on the wing surface. As a result, a reduction of about 56% on the overall drag force is reported for the controlled case. As the angle

Figure 17: Contours of pressure coefficient (upper column) and friction lines distribution (lower column) on wing suction side surface at flow conditions of $\alpha = 11°$ and $Re_c = 4.45 \times 10^5$; (a) baseline case; (b) controlled case (flow moving top to bottom).

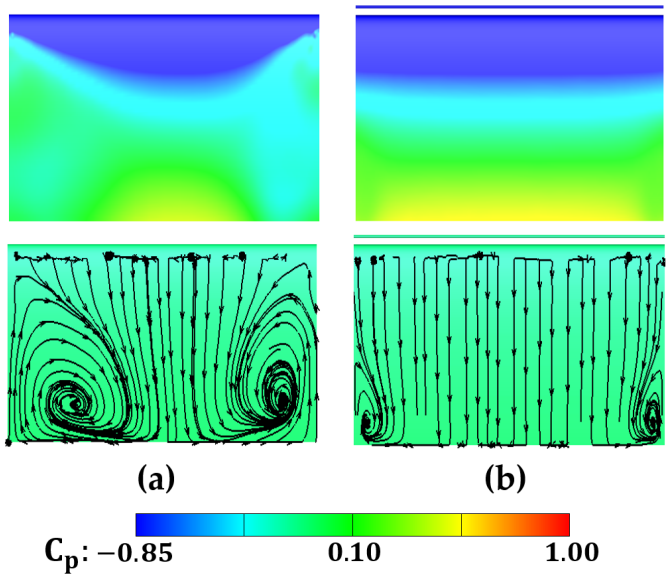

of attack is increased the instability amplifies more and more to form two large counter-rotating vortices covering a large part of the wing upper surface. A backflow is generated as a consequence of these two vortices. This reveals that energy of the incoming flow is more dominant than

that of the backflow. As a result of this dominance the incident flow imposed its presence mainly in the midspan zone, hence, the boundary layer is not completely separated from the wing surface except in the region where the vortices are present. For $\alpha = 12°$, direction of friction lines on the midspan zone shows that the backflow becomes dominant and imposes its presence with respect to the incoming flow. The two counter-rotating vortices still exist, but larger in dimensions and intensities when compared to those observed for incidence $\alpha = 11°$. Therefore, secondary instabilities appear as a consequence of this interaction between the two flows of opposite sense and the significant energy of this backflow, Fig.18.In this case, the boundary layer is completely separated from the wall. This irregularity behind appearance of this instability disturbs the uniform distribution of the average pressure in both ends of the wing close to the leading edge. However, when flow control is applied, the average pressure distribution becomes uniform and homogeneous and the disturbed zones near the endplates vanish. In addition, this depression portion grows in size compared to previous angles. Moreover, presence of the rod has a significant impact on the flow developing on the wing suction side. From the Fig.18 it is easily noticeable that secondary instabilities reported before completely disappear and the incoming flow gained energy from the feeding vortex generator to become dominant over a large portion of the wing because it overpassed the early backflow seen without control. As a consequence, the two counter-rotating vortices died out and straitened in size resulting a reduction in the drag force by 73% including the rod contribution. For incidence greater than 12°, the uniform distribution of the

Figure 18: Contours of pressure coefficient (upper column) and friction lines distribution (lower column) on wing suction side surface at flow conditions of $\alpha = 12°$ and $Re_c = 4.45 \times 10^5$; (a) baseline case; (b) controlled case (flow moving top to bottom).

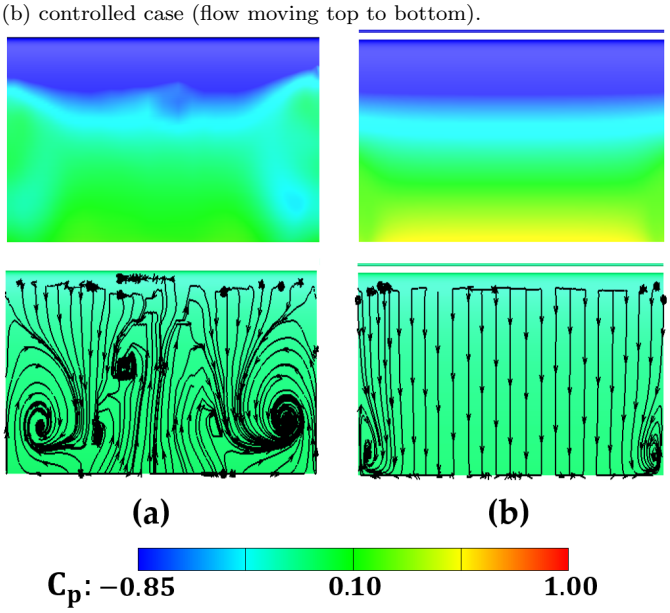

mean pressure over the entire upper surface is completely disturbed for the baseline configuration, Fig.19. Consequently, the flow within the boundary layer is completely unstable. The intensity of these instabilities increases with the angle of attack causing the so-called turbulent stall to launch. As α increases, these instabilities are intensified and the boundary layer separation is generalized to the entire wing surface. For $\alpha = 13°$ the flow seems to behave in the same way as for 12° incidence without control. This is clearly shown by friction lines pattern, where the dominance of the backflow resulting from instabilities generated inside the boundary layer is well represented leading to secondary irregularities as a result of the interaction between the incident and back flows. In this case, the boundary layer is completely detached from the surface and this incident angle corresponds to the turbulent and massive stall angles of the flow. In the other hand, as the control technique is applied, the mean pressure distribution on the suction side of the wing exhibits a different behaviour in comparison to the baseline case. As stated earlier, the mean pressure distribution is random due to partial separation of the boundary layer near endplates caused by the primary and secondary vortices that gain intensity to cover an important portion of the wing surface as illustrated in friction lines patterns showing dominance of the backflow over the incoming one. Thereby, presence of the vortex generator brought the depression zone near the leading edge from its randomness attitude to its uniform and homogenous shape similar to what was observed at lower angles of attack when control is absent. It is worthwhile noting from pressure contours that flow characteristics are delayed by 2° from the baseline configuration with flow control applied. In other words, the stall is postponed when the wing is operating in the rod wake. In fact, looking at the new pattern of friction lines after low control is set, what have been seen in average pressure distribution is emphasized throughout the assessment of the flow before and after the control. As a matter of fact, the wake produced by the rod evolves into shedded eddies interacting with the boundary layer developing on the wing upper surface in a way that they feed energy to the flow close to the wall from free-stream. Premature separated boundary layer is reinforced to overcome pressure gradients that is subjected to and stick again to the wall surface. Consequently, this phenomenon of energizing the upcoming flow is established by defeating the dominance of the backflow spotted in the baseline case, so that the flow recovered its chordwise direction mostly in the midspan portion of the wing. Although the pair of vortices remain near the endplates a part of consequence of three-dimensionalities attitude of the flow outcomes of interferences between the two boundary layers developing on either endplates and wing body, the secondary instabilities are completely vanished for the controlled case. To sum up this qualitative analysis that provides main differences on the flow structures before and after control, it is important to link these essential findings to their impact on aerodynamic loads

specifically lift and drag forces. It is found that actual aerodynamic coefficients are highly sensitive to flow control in an extent of a lift enhancement of 17% to gather with a maximum drag reduction of 49% which is promising in a perspective of fineness improvement. Figure 20

Figure 19: Contours of pressure coefficient (upper column) and friction lines distribution (lower column) on wing suction side surface at flow conditions of $\alpha = 13°$ and $Re_c = 4.45 \times 10^5$; (a) baseline case; (b) controlled case (flow moving top to bottom).

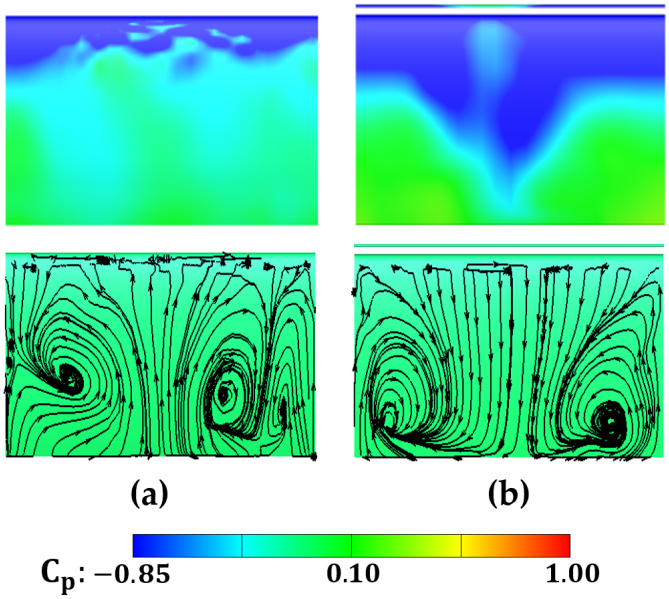

depicts mean surface pressure distribution on the suction side generated by the wing operating in the low Reynolds number condition and at 15° incidence angle. For the non-controlled case the surface pressures appear very instable, as expected, whilst at such high angle of attack a presence of an intense turbulent agitation of the flow within the boundary layer is naturally understandable as turbulent stall of the boundary layer has taken place. This is shown on the friction lines illustration (bottom right-hand column), which reveal in the low-pressure regions near endplates formation of a pair of counter rotating vortices due to circulation of flow from higher to lower pressure regions. Also, when looking at the evolution way of these lines going from the trailing edge towards the leading edge over the entire wing surface is an evidence on the backflow dominance over the incoming stream. Similarly, to what have been described in the previous angle of attack, the boundary layer is fully separated from the wing upper surface giving rise to a wing stalled state. In other hand, a micro rod is used for prospective wing performances enhancement. Some relevant findings are presented in the left-hand column of the Fig.20. The instabilities in the average pressure distribution seem to be damped down to an extent where uniformity and homogenous appearance is recovered close to the leading edge. An analogy of this pressure contour with the baseline case, turns up this flow pattern resulting from the control device is already seen at earlier angle of attack, 11°. This inferred that this passive control delays heavy stall by few degrees. There appear to be larger area of low pressure in the mid-span region of the wing as the main flow gain control over the backflow and sticks to the wing again through involvement of rod eddies that convey energy from free-stream to boundary layer. Whereas, close to the endplates, less suction is generated as the three-dimensional interfaces in the boundary layers of these two regions arise tiny secondary instabilities on both sides that block the flow from it. To complete what is said so far, friction lines on the upper surface of the wing at 15° incidence with flow control are also considered. It is found that the flow got back its streamwise direction in comparison to the baseline case. This is because the boundary layer is completely separated from the wall and reattach to the wing particularly in the mid-span region constraining the stream to flow downward to the trailing edge. Two thirds of the wing suction side are occupied by a pair of counter rotating vortices resulting from recirculation of the flow from high to low pressure. In addition of secondary instabilities close to the leading edge on both sides are generated the flow from the endplates interferes with the wing boundary layer, which yield it to partially stalled state. Finally, all these results conclusively show that passive control as uses here showed capability to delay full stall by 3°. Furthermore, an enhancement in aerodynamic loads is also ensured with control. 21% of drag reduction and 23% in lift growth are effectively obtained.

Figure 20: Contours of pressure coefficient (upper column) and friction lines distribution (lower column) on wing suction side surface at flow conditions of $\alpha = 15°$ and $Re_c = 4.45 \times 10^5$; (a) baseline case; (b) controlled case (flow moving top to bottom).

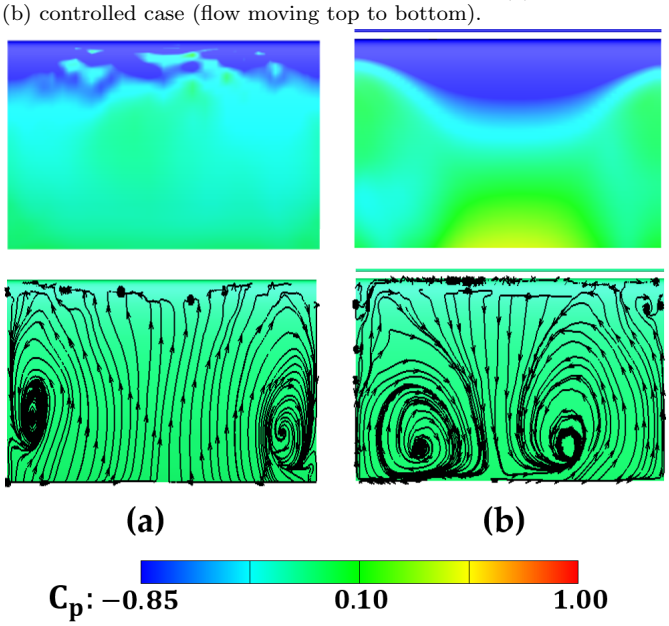

4. Conclusion

In this paper a passive flow control approach for a pre-stalled and post-stalled aerofoil is numerically investigated. Flow response to placing a microcylindrical shaped rod near NACA0012 wing-based profile at low chord-based Reynolds number of $Re_c = 4.45 \times 10^5$ is carefully examined. Particular focus is put on parietal pressure distribution on suction side surface along with flow field patterns with corresponding impart on the overall aerodynamic loads particularly high angles of attack ranging from 0° to 24°. The longitudinal gap between the wing and rod together with rod's diameter are key parameters carefully considered in this study. Detailed RANS CFD calculations are carried out for both controlled and baseline cases to show the influence of the joint device on the flow control effectiveness. Friction lines are further analysed to give information on the flow field behaviour on wall surface and correlative pressure distribution. The diameter of the microcylindrical rod considered for this current study is $d/c = 0.013$, placed away from the wing leading edge at 3 times the diameter in the chordwise direction. For the baseline case, flow fields and average pressure coefficient distribution analysis made it possible to highlight the underlying physical phenomenology involved in laminar and turbulent boundary layer separation. It is shown that laminar boundary layer is particularly sensitive to pressure gradients induced by the wing at incidence. This caused premature separation of the flow followed by reattachment after transition to turbulent state accompanied by formation of the so-called laminar separation bubble (LSB). At the pre-stall flow condition ($\alpha < 13°$), the bubble forms near the trailing edge of the wing. As the incidence increases the LSB significantly decreases in length while migrating upstream to stabilize in the vicinity of the leading edge. This feature is encountered between $\alpha = 2°$ and $\alpha = 8°$. When the angle of attack is greater than 8°, the aerofoil exhibits presence of a second conventional bubble near the trailing edge as well as the LSB near the leading edge. At $\alpha = 12°$ the laminar flow completely separates from the wing upper surface and forming a large recirculation zone; hence the wing is stalled. Any further increase in incidence results in the laminar separation bubble sudden burst leading to a heavy turbulent separation of the boundary layer subsequently to the important pressure gradient. Analysis of lift and drag forces with the LBS formed showed significant degradation in the overall aerodynamic loads pushing the wing to an abrupt stall. When the microcylindrical control device is introduced into the flow, a considerable influence on the behaviour of the laminar separation bubble is induced. Presence of the rod revealed ability to partially eliminate the bubble by causing an early reattachment of the premature laminar separated boundary layer over a significant extent. The total length of the LSB is found to reduce by more than 75% and almost vanish for an incidence of 10° (Table 5).

Figure 21: Contours of pressure coefficient (upper column) and friction lines distribution (lower column) on wing suction side surface at flow conditions of $\alpha = 10°$; $Re_c = 4.45 \times 10^5$ and diffrent rods' size (flow moving top to bottom).

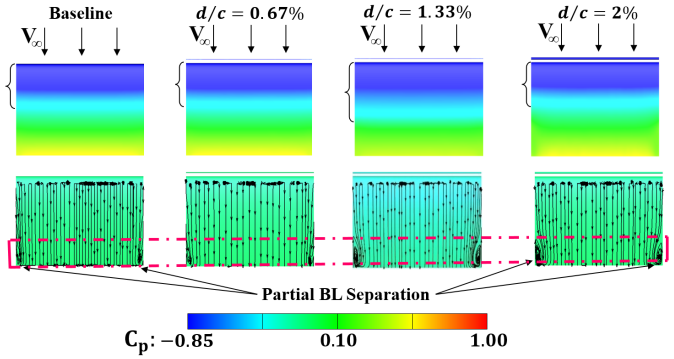

Figure 22: Contours of pressure coefficient (upper column) and friction lines distribution (lower column) on wing suction side surface at flow conditions of $\alpha = 11°$; $Re_c = 4.45 \times 10^5$ and diffrent rods' size (flow moving top to bottom).

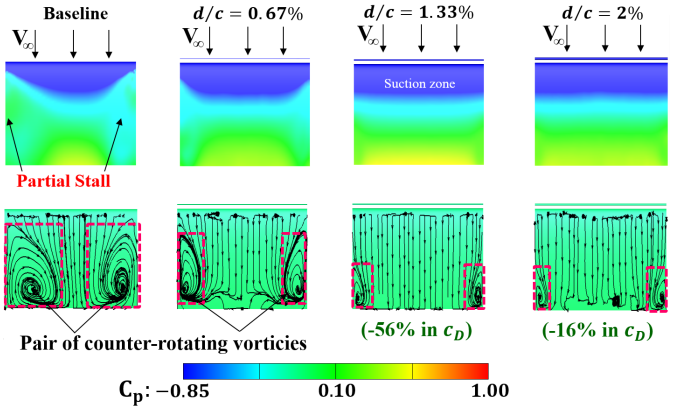

Figure 23: Contours of pressure coefficient (upper column) and friction lines distribution (lower column) on wing suction side surface at flow conditions of $\alpha = 12°$; $Re_c = 4.45 \times 10^5$ and diffrent rods' size (flow moving top to bottom).

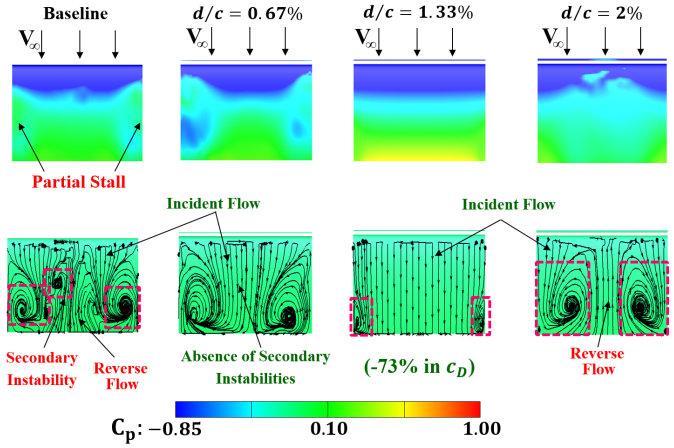

Figure 24: Contours of pressure coefficient (upper column) and friction lines distribution (lower column) on wing suction side surface at flow conditions of $\alpha = 13°$; $Re_c = 4.45 \times 10^5$ and diffrent rods' size (flow moving top to bottom).

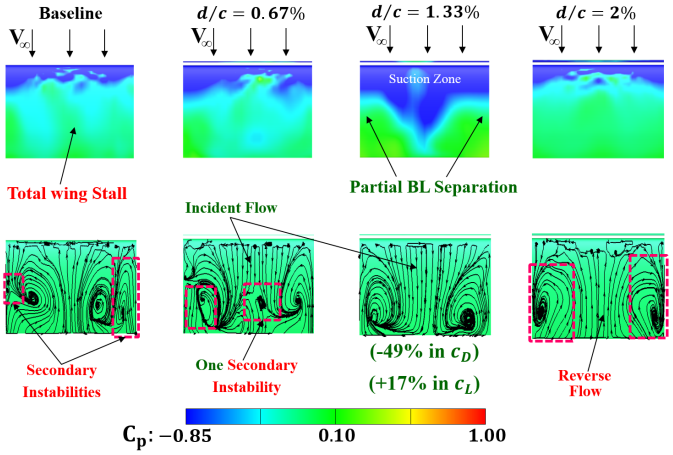

Figure 25: Contours of pressure coefficient (upper column) and friction lines distribution (lower column) on wing suction side surface at flow conditions of $\alpha = 15°$; $Re_c = 4.45 \times 10^5$ and diffrent rods' size (flow moving top to bottom).

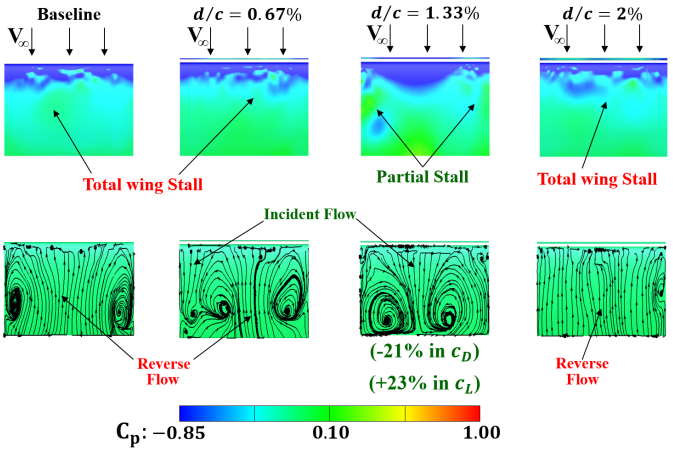

Furthermore, the vortex like generator deeply impacts the flow structure especially at stall and post-stall conditions. At AOAs ranged between 10° to 15°, the control device acts similarly to a pumping system energizing the boundary layer on the aerofoil counter-balancing the adverse pressure gradients. In fact, eddies generated in the cylinder wake interact with the boundary layer of the wing, ensuring convection of energy from freestream to near wall flow. The size of the downstream recirculation zone is significantly reduced for post-stall conditions. In other words, mean pressure contours and corresponding friction lines on the suction side are corroborating results for control effectiveness of the rod beyond stall conditions of the baseline wing. It was capable of maintaining attached flow for incidence of 15° till 33% of the whole wing upper surface close to the midspan region, while the backflow took advantage in non-controlled configuration, hence a complete separation from the leading edge was noticed. Finally, for pre-stall regime, the controlled flow doesn't provide significant improvement in either lift and drag, but does show effectiveness in reducing the length of the laminar separation bubble leading to further understanding of the intricate involved dynamics influencing the wing aerodynamic performances. Meanwhile, at post-stall regime presence of the rod close to the leading edge seems to effectively suppress or diminish and in most favourable case delay flow separation to higher angles of attack. This is advantageous to either lift enhancement or drag reduction, resulting respectively in a gain of 23% and a reduction of 73% (Fig.24 and Fig.25)as evaluated in this study (Fig.22 and Fig.23).

References

[1] Aguedal, L., Semmar, D., Berrouk, A.S., Azzi, A. and Oualli, H. (2018) '3D Vortex Structure Investigation using Large Eddy Simulation of Flow around a Rotary Oscillating Circular Cylinder', *European Journal of Mechanics-B/Fluids*, Vol. 71, pp. 113–125

[2] Aldheeb, M., Asrar, W., Omar, A.A., Altaf, A. and Sulaeman, E. (2020) 'Aerodynamics of Symmetric Permeable Airfoils and Wings: CFD Simulation', *Progress in Computational Fluid Dynamics, an International Journal*, Vol. 20, No. 6, pp. 349–362

[3] Bajalan, S., Shadaram, A., Hedayat, N. and Taleghani, A. S. (2011) 'Experimental Study of Frequency Behavior for a Circular Cylinder behind an Airfoil', *World Academy of Science, Engineering and Technology, International Journal of Mechanical, Aerospace, Industrial, Mechatronic and Manufacturing Engineering*, Vol. 5, No. 11, pp. 2356–2360

[4] Benim, A.C. and Diederich, M. (2019) 'Prediction of Roughness Effects on Wind Turbine Aerodynamics', *E3S Web of Conferences, Edp Science*, Vol. 128, pp. 09004

[5] Colonia, S., Leble, V., Steijl, R. and Barakos, G. (2017) 'Assessment and Calibration of the γ-Equation Transtion Model at Low Mach', *AIAA Journal*, Vol. 55, No. 4, pp. 1126–1139

[6] Critzos, C.C., Heyson, H.H. and Boswinkle, R.W. (1955) 'Aerodynamic Characteristics of a NACA0012 Airfoil Section at Angles of Attack from 0deg to 180deg', *NACA Technical Report, National Aeronautics and Space Administration, Washington DC*, Vol. NACA-TN3361

[7] Durhasan, T. (2020) 'Passive Flow Control over an Airfoil by Control Rod at Low Reynolds Number', *Journal of Applied Fluid Mechanics*, Vol. 13, No. 6, pp. 1819–1833

[8] Fatahian, E., Nichkoohi, A. L., and Fatahian, H. (2019) 'Numerical Study of the Effect of Suction at a Compressible and High Reynolds Number Flow to Control the Flow Separation over NACA2415 Airfoil', *Progress in Computational Fluid Dynamics, an International Journal*, Vol. 19, No. 3, pp. 170–179

[9] Gad-el-Hak, M. (2000) 'Flow Control: Passive, Active, and Reactive Flow Management', *Cambridge University Press, Cambridge, UK*, pp. 112, 151–152, 163, 176

[10] Gupta, A. and Saha, A.K. (2019) 'Suppression of Vortex Shedding in Flow around a Square Cylinder using Control Cylinder', *European Journal of Mechanics-B/Fluids*, Vol. 76, pp. 276–291

[11] Hafien, C., Bourehla, A. and Bouzaien, M. (2016) 'Passive Separation Control on a Symmetric Airfoil via Elastic-Layer', *Journal of Applied Fluid Mechanics*, Vol. 9, No. 5, pp. 2569-2580

[12] Hain, R., Kähler, C.J. and Radespiel, R. (2009) 'Dynamics of Laminar Separation Bubbles at Low-Reynolds-Number Aerofoils', *Journal of Fluid Mechanics*, Vol. 630, pp. 129–153

[13] Hu, H. and Yang, Z. (2008) 'An experimental Study of the Laminar Flow Separation on a Low-Reynolds-Number Airfoil', *Journal of Fluids Engineering*, Vol. 130, No. 5, pp. 051101

[14] Huang, L., Huang, P.G., LeBeau, R.P. and Hauser, T.h. (2004) 'Numerical Study of Blowing and Suction Control Mechanism on NACA0012 Airfoil', *Journal of Aircraft*, Vol. 41, No. 5, pp. 1005–1013

[15] Igarashi, T. and Tsutsui, T. (1998) 'Enhancement of Heat Transfer and Reduction of Drag of a Square Prism Arranged Diamond-Shape in an Air Stream', 11^{th} *International Heat Transfer Conference, Kyongiu, Korea*, Vol. 5, pp. 261–266

[16] Igarashi, T. (1994) 'Enhancement of Heat Transfer and Reduction of Drag of a Square Prism in an Air Stream', 10^{th} *International Heat Transfer Conference, Brighton*, Vol. 6, pp. 49–54

[17] Igarashi, T. (1997) 'Drag Reduction of a Square Prism by Flow Control using a Small Rod', *Journal of Wind Engineering and Industrial Aerodynamics*, Vol. 69-71, pp. 141–153

[18] Jacobs, E.N. and Sherman, A. (1937) 'Airfoil Section Characteristics as Affected by Variations of the Reynolds Number', *NACA Technical Report*, Vol. 586, pp. 227–267

[19] Langtry, R. B. and Menter, F. R. (2009) 'Correlation-Based Transition Modeling for Unstructured Parallelized Computational Fluid Dynamics Codes', *AIAA Journal*, Vol. 47, No. 12, pp. 2894–2906

[20] Lei, C., Cheng, L. and Kavanagh, K. (2001) 'Spanwise Length Effects on Three-Dimensional Modelling of Flow over a Circular Cylinder', *Computer Methods in Applied Mechanics and Engineering*, Vol. 190, No. 22–23, pp. 2909–2923

[21] Li, D., Liu, Y., Li, G., Xie, L. and Sun, L. (2019) 'Airfoil Noise Reduction using Boundary Layer Control', *Progress in Computational Fluid Dynamics, an International Journal*, Vol. 19, No. 2, pp. 98–108

[22] Malan, P., Suluksna, K. and Juntasaro, E. (2009) 'Calibrating the $\gamma - \tilde{Re}_\theta$ Transition Model for Commercial CFD', 47^{th} *Aerospace Sciences Meeting Including, the New Horizons Forum and Aerospace Exposition, AIAA, Orlando, Florida*, Report No. 2009–1142

[23] Menter, F.R., Langtry, R.B., Likki, S.R., Suzen, Y.B., Huang, P.G. and Volker, S. (2006) 'A Correlation-Based Transition Model using Local Variables-Part I: Model Formulation', *ASME Journal of Turbomachinery*, Vol. 128, pp. 413–422

[24] Michelis, T. and Kotsonis, M. (2015) 'Interaction of an Off-Surface Cylinder with Separated Flow from a Bluff Body Leading Edge', *Experimental Thermal and Fluid Science*, Vol. 63, pp. 91–105

[25] Mitchell, S., Ogbonna, I. and Volkov, K. (2021) 'Aerodynamic Characteristics of a Single Airfoil for Vertical Axis Wind Turbine Blades and Performance Prediction of Wind Turbines', *Fluids*, Vol. 6, No. 7, pp. 257

[26] Norberg, C. (1998) 'LDV-Measurements in the Near Wake of a Circular Cylinder', *Proceedings of the Conference on Bluff Body Wakes and Vortex Induced Vibration, Washington DC, Edited by P.W. Bearman and C.H.K. Williamson (Cornell University, Ithaca, NY)*, pp. 1–12

[27] Ripley, M. D. and Pauley, L. L. (1993) 'The Unsteady Structure of Two-Dimensional Steady Laminar Separation', *Physics of Fluids A: Fluid Dynamics*, Vol. 5, No. 12, pp. 3099–3106

[28] Roberts, L.S. (2017) 'Boundary-Layer Transition on Wings in Ground Effect', *PhD Thesis, Cranfield University*

[29] Russell, J. M. (1979) 'Length and Bursting of Separation Bubbles: A Physical Interpretation of Pressure Distribution', *NASA. Langley Research Center; The Science and Technolgy of Low Speed and Motorless Flight, Part 1 Cambridge, MA, USA*, pp. 177–202

[30] Sefiddashti, M. N., Nili-Ahmadabadi, M. and Rizi, B. S. (2018) 'Experimental Study of Effects of Circular-Cross-Section Riblets on the Aerodynamic Performance of Risø Airfoil at Transient Flow Regime', *Journal of Mechanical Science and Technology*, Vol. 32, No. 2, pp. 709–716

[31] Shan, H., Jiang, L., Liu, C., Love, M., and Maines, B. (2008) 'Numerical Study of Passive and Active Flow Separation Control over a NACA0012 Airfoil', *Computers & Fluids*, Vol. 37, No. 8, pp. 975–992

[32] Steed, R.G.F. (2011) 'High Lift CFD Simulations with an SST-Based Predictive Laminar to Turbulent Transition Model', 49^{th} *AIAA Aerospace Science Meeting including the New Horizons Forum and Aerospace Exposition, Orlando, Florida*, Paper 2011-0864, January 2011

[33] Strykowski, P.J. and Sreenivasan, K.R. (1990) 'On the Formation and Suppression of Vortex Shedding at Low Reynolds Numbers', *Journal of Fluid Mechanics*, Vol. 218, pp. 71–107

[34] Supreeth, R., Arokkiaswamy, A., Anirudh, K., Pradyumna, R.K., Pramod, PK. and Sanarahamat, A.K. (2020) 'Experimental and Numerical Investigation of the Influence of Leading Edge Tubercles on S823 Airfoil Behavior', *Journal of Applied Fluid Mechanics*, Vol. 13, No. 9, pp. 1885–1899

[35] Tani, I. (1964). 'Low-Speed Flows Involving Bubble Separations', *Progress in Aerospace Sciences*, Vol. 5, pp. 70–103

[36] Tong, F., Qiao, W., Chen, W., Haoyi, C., Wei, R. and Wang, X. (2018) 'Numerical Analysis of Broadband Noise Reduction with Wavy Leading Edge', *Chinese Journal of Aeronautics*, Vol.31, No. 7, pp. 1489–1505

[37] Vuddagiri, A., Halder, P., Samad, A. and Chaudhuri, A. (2016) 'Flow Analysis of Airfoil having Different Cavities on its Suction Surface', *Progress in Computational Fluid Dynamics, an International Journal*, Vol. 16, No. 2, pp. 67–77

[38] Wang, Y., Li, G., Shen, S., Huang, D. and Zheng, Z. (2018) 'Influence of an Off-Surface Small Structure on the Flow Control Effect on Horizontal Axis Wind Turbine at Different Relative Inflow Angles', *Energy*, Vol. 160, pp. 101–121

[39] Yang, Z. and Voke, P.R. (2001) 'Large-Eddy Simulation of Boundary-Layer Separation and Transition at a Change of Surface Curvature', *Journal of Fluid Mechanics*, Vol. 30, No. 3, pp. 439–305

[40] Zhang, X., Mahallati, A., and Sjolander, S. (2002) 'Hot-Film Measurements of Boundary Layer Transition, Separartion and Reattachment on a Low-Pressure Turbine Airfoil at Low Reynolds Numbers', 38^{th} *AIAA/ASME/SAE/ASEE Joint Propulsion Conference & Exhibit*, pp. 3643–3655

[41] Zhang, H.J., Huang, L. and Zhou, Y. (2005) 'Aerodynamic Loading on a Cylinder behind an Airfoil', *Experiments in Fluids*, Vol. 38, No. 5, pp. 588–593

[42] Zhou, C.Y., Sun, C.W., Zhou, Y. and Huang, L. (2004) 'A Numerical Study of a Circular Cylinder in the Wake of an Airfoil', 15^{th} *Australasian Fluid Mechanics Conference, University of Sydney, Sydney, Australia*, pp. 13–17

Nomenclature

Latin Symbols	
$AOAs$	Angles Of Attack
c	Chord length
c_D	Drag coefficient
c_L	Lift coefficient
C_p	Pressure coefficient
cov	Covariance
d	Rod diameter
k	Turbulent kinetic energy
L	Distance between the Rod and LE
LE	Leading Edge
l_f	Formation length
LSB	Laminar Separation Bubble
L_z	CFD domain spanwise length
Re	Reynolds number
$Re_{\theta,c}$	Re number where fluctuations begin
$Re_{\theta,t}$	Re number where transition occurs
SST	Shear Stress Transport
t	Time
$\mathbf{U}$	Velocity field
V_∞	Freestream velocity
X	Data set
Y	Data set
y^+	Non-dimentional wall distance
$3D$	Three-Dimensional
Greek Symbols	
α	Angle of attack
ϵ	Turbulent dissipation rate
γ	Intermittency
ω	Specific dissipation rate
σ	Standard deviation